Syntaxin 3 regulates apical membrane integrity in proximal tubule epithelial cells and prevents Fanconi syndrome development

OPEN

Hiroki Okushima[1,10], Kazunori Inoue[1,10], Atsuhiro Imai[1], Ayumi Matsumoto[1], Natsune Tamai[1], Masataka Kunii[2], Nobuhisa Iriuchijima[3], Rüdiger Adam[4], Yusriya Al Rawahi[5], Siham Al Sinani[6], Takeshi Yamamoto[1], Masayuki Mizui[1], Akihiro Harada[2], Motoko Yanagita[7,8], Yoshitaka Isaka[1] and Isao Matsui[1,9]

[1]Department of Nephrology, Graduate School of Medicine, The University of Osaka, Suita, Osaka, Japan; [2]Department of Cell Biology, Graduate School of Medicine, The University of Osaka, Suita, Osaka, Japan; [3]Department of Anesthesiology, Kiryu Kosei General Hospital, Orihime-cho, Kiryu, Gunma, Japan; [4]University Children's Hospital, Pediatric Gastroenterology, Hepatology and Nutrition, Medical Faculty Mannheim, Heidelberg University, Mannheim, Germany; [5]Child Health Department, Sultan Qaboos University Hospital, University Medical City, Muscat, Oman; [6]University Medical City, Muscat, Oman; [7]Department of Nephrology, Graduate School of Medicine, Kyoto University, Kyoto, Japan; [8]Institute for the Advanced Study of Human Biology, Kyoto University, Kyoto, Japan; and [9]Transdimensional Life Imaging Division, Institute for Open and Transdisciplinary Research Initiatives, The University of Osaka, Suita, Osaka, Japan

Abstract

Introduction: Epithelial cell polarity is crucial for the proper functioning of various organs, including the kidneys. Syntaxin 3, a key molecule in membrane-vesicle fusion, is localized in the apical membrane of proximal tubule epithelial cells (PTECs). Although *in vitro* studies using the other type of epithelial cells besides PTECs have shown the role of syntaxin 3 in regulating apical membrane integrity, its function in epithelial cells *in vivo*, particularly in PTECs, remains undefined.

Methods: We analyzed the renal phenotypes of a newly generated PTEC-specific *Stx3* knockout mice (*Stx3*-cKO) and examined urine samples from patients with microvillus inclusion disease (MVID) carrying *STX3* mutations.

Results: *Stx3*-cKO mice exhibited features of Fanconi syndrome, including increased urinary excretion of phosphorus, glucose, amino acids, and low-molecular-weight proteins. Patients with MVID showed similar urinary abnormalities. The mice exhibited brush border atrophy and vesicle transport stagnation, as evidenced by electron microscopy, and increased subapical localization of trafficking markers, Rab11 and vesicle-associated membrane protein 8. Key transporters and receptors including sodium-dependent phosphate cotransporter type 2a, sodium-glucose cotransporter 2, a protein related to the neutral and basic amino acid transport protein rBAT, and megalin showed mislocalization and/or altered expression. Syntaxin 3 deficiency disrupted the apical expression of ezrin, a crucial protein that links the actin cytoskeleton to the plasma membrane. Both receptor-mediated and fluid-phase endocytosis were impaired in *Stx3*-cKO mice.

Conclusions: Our results highlight the critical role of syntaxin 3 in maintaining PTEC function and apical polarity, providing new insights into the kidney manifestations of MVID and the molecular mechanisms underlying Fanconi syndrome.

Kidney International (2025) **108,** 1088–1104; https://doi.org/10.1016/j.kint.2025.08.027

KEYWORDS: apical membrane; Fanconi syndrome; microvillus inclusion disease; polarity; proximal tubules; syntaxin 3

Translational Statement

This study reveals the critical role of syntaxin 3 in preventing Fanconi syndrome. Our findings in both mouse models of *Stx3* conditional knockout and patients with microvillus inclusion disease (MVID) carrying *STX3* mutations highlight the potential kidney manifestations of MVID, which may be overlooked in clinical settings. This study suggests that patients with MVID carrying *STX3* mutations should be monitored for Fanconi syndrome. Furthermore, our mechanistic insights into the function of syntaxin 3 may guide future therapeutic strategies for Fanconi syndrome and other tubular disorders. The next step involves exploring targeted interventions to mitigate kidney manifestations of syntaxin 3 dysfunction.

Correspondence: *Masataka Kunii, Department of Cell Biology, Graduate School of Medicine, The University of Osaka, 2-2 Yamada-oka, Suita, Osaka 565-0871, Japan. E-mail: mstk921@acb.med.osaka-u.ac.jp; or Isao Matsui, Department of Nephrology, Graduate School of Medicine, The University of Osaka,2-2 Yamada-oka, Suita, Osaka 565-0871, Japan. E-mail: matsui@kid.med.osaka-u.ac.jp*

[10]HO and KI contributed equally to this work.

Received 27 December 2024; revised 24 July 2025; accepted 22 August 2025; published online 29 September 2025

The proximal tubule (PT) is a critical segment of the kidney nephron and is responsible for reabsorbing most essential nutrients, ions, and low-molecular-weight proteins from the glomerular filtrate.[1] This process is mediated by various transporters and endocytic receptors specifically expressed on the apical membranes of PT epithelial cells (PTECs).[2–4] The mislocalization of these proteins can lead to Fanconi syndrome.[5] Despite the clinical significance of proper protein localization in PTECs, the molecular mechanisms governing these processes remain unclear.

Syntaxin 3, a protein encoded by the *Stx3* gene in mice and the *STX3* gene in humans, plays a crucial role in localizing apical membrane proteins in epithelial cells.[6,7] This function has been primarily demonstrated by *in vitro* experiments using cultured epithelial cell models, in which syntaxin 3 forms soluble N-ethylmaleimide–sensitive factor attachment protein receptor (SNARE) complexes that facilitate membrane fusion and vesicle content delivery to the apical surface.[6,8–10] The importance of syntaxin 3 *in vivo* was underscored by 2 key observations. First, systemic *Stx3* knockout mice exhibit embryonic lethality, highlighting the critical role in development.[11] Second, mutations in *STX3* cause human disease with variable phenotypes. In humans, *STX3* exists as 2 isoforms: *STX3A*, which is expressed in multiple tissues, including intestine, retina, kidney, and pancreas, and the retina-specific *STX3B*.[12] Biallelic mutations affecting only *STX3A* result in microvillus inclusion disease (MVID), characterized by severe intestinal malabsorption and morphologic abnormalities in the intestinal epithelium.[12,13] When mutations affect both *STX3A* and *STX3B* transcripts, patients develop a syndromic form of MVID accompanied by severe retinal dystrophy.[12] The location of variants within the gene determines not only which organs are affected, but also influences the severity and onset timing of both intestinal and eye-related manifestations.[12]

In mouse kidneys, syntaxin 3 is predominantly localized in the apical membranes of PTECs.[6,14] Although the intestinal phenotype of patients with MVID caused by *STX3* mutations has been characterized by *in vitro* experiments and clinical observations, the specific role of syntaxin 3 in epithelial cells *in vivo* remains largely unexplored.[12,13] This gap in our understanding is particularly significant given that conditional knockout studies of *Stx3* have primarily focused on neuronal populations, including retinal rod cells, another cell type where syntaxin 3 function has been studied.[12,15] Although these conditional knockout studies in neurons have provided valuable insights, they highlight the lack of in-depth investigation into the specific function of syntaxin 3 in epithelial tissues. Among the various epithelial cell types, we specifically focused on PTECs in this study for the following key reasons: (i) the unexplored kidney manifestations of syntaxin 3 dysfunction in MVID, (ii) the potential role of syntaxin 3 in maintaining PTEC function and preventing Fanconi syndrome development, and (iii) the opportunity to uncover the fundamental mechanisms of apical membrane organization in epithelial cells *in vivo*.

To elucidate the specific function of syntaxin 3 in PTECs *in vivo*, we generated tamoxifen-inducible, PTEC-specific *Stx3* knockout mice. We hypothesized that syntaxin 3 deficiency disrupts apical membrane integrity, potentially leading to a Fanconi syndrome phenotype. This study aimed to provide new insights into the role of syntaxin 3 in kidney function and the pathophysiology of Fanconi syndrome and MVID.

METHODS

Clinical sample analysis

Blood and urine samples from 2 patients with MVID carrying *STX3* gene mutations were analyzed for Fanconi syndrome–related parameters. Estimated glomerular filtration rate was calculated by the creatinine-based Bedside Schwartz equation.[16] The patients were under follow-up care at University Medical Centre Mannheim (Germany) and the Sultan Qaboos University Hospital (Oman). The study was approved by the Ethical Review Committee of The University of Osaka Hospital (approval number: 23105), and written informed consent was obtained from the participants.

Animal experiments

Mice were housed in a humidity-controlled specific pathogen-free room maintained at 22 °C to 24°C with a 12-hour light/dark cycle. All mice had *ad libitum* access to water and a standard diet (MF diet; Oriental Yeast) containing 1.07% calcium and 0.83% phosphorus. For invasive procedures, the mice were anesthetized using i.p. injections of medetomidine, midazolam, and butorphanol. All animal experiments were approved by the Animal Ethics Committee of The University of Osaka (approval number: 04-059) and were conducted in accordance with the National Institutes of Health guidelines for laboratory animal care and use. The number of animals used was determined on the basis of the 3Rs principles (replacement, reduction, and refinement). To minimize potential confounding factors, the order of the blood and urine tests and animal cage arrangements were randomized.

Mouse strains and genetic modification

For experiments labeled as "WT mouse kidney" in Figure 1, wild-type (WT) C57BL/6J mice (8 weeks old; Japan SLC) were used. All other experiments were performed using genetically modified mice with the C57BL/6 genetic background. $Stx3^{fl/fl}$ mice were generated essentially as previously described (Supplementary Methods).[17] $Ndrg1^{CreERT2/+}$ transgenic mice were generated as previously described.[18] $Stx3^{fl/fl}$ mice were crossed with $Ndrg1^{CreERT2/+}$ mice to generate $Stx3^{fl/fl}$;$Ndrg1^{CreERT2/+}$ mice. To induce Cre expression under the control of the *Ndrg1* promoter in adult mice, 8-week-old $Stx3^{fl/fl}$;$Ndrg1^{CreERT2/+}$ mice were i.p. injected with 0.15 mg/g body weight tamoxifen (Sigma Aldrich) dissolved in corn

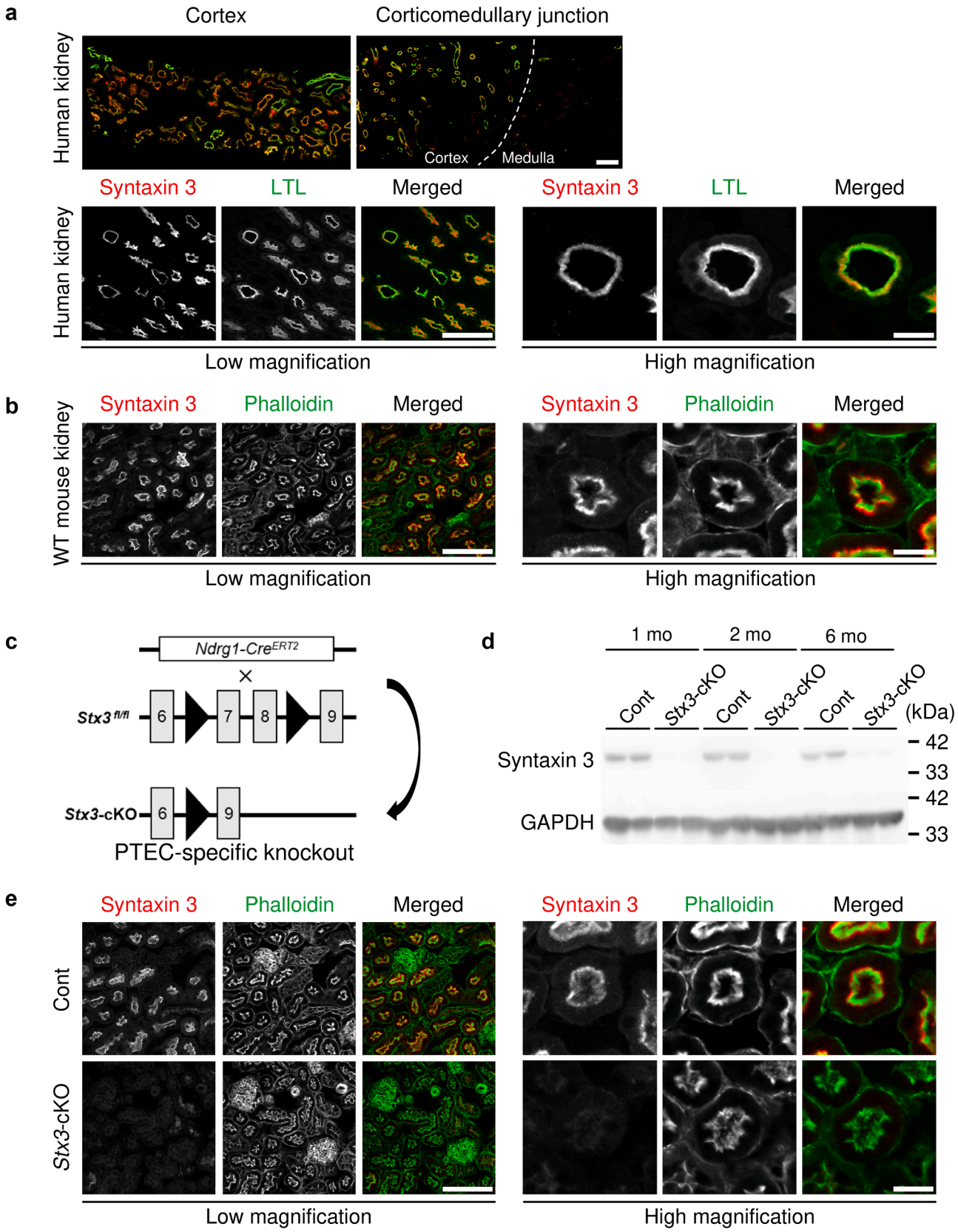

Figure 1 | Syntaxin 3 expression and localization in human and mouse kidney tissues, and generation of proximal tubule epithelial cell (PTEC)–specific *Stx3* conditional knockout (*Stx3*-cKO) mice. (**a**) Immunofluorescence staining of human kidney biopsy tissue. Upper panels show the cortex (left) and corticomedullary junction (right) at a magnification allowing distinction of these regions, with a dashed line indicating the corticomedullary border. Lower panels display cortical regions at low (left) and high (right) (continued)

oil (Sigma Aldrich) every other day for a total of 3 injections. These conditional knockout mice were referred to as *Stx3*-cKO. Age-matched *Stx3*$^{fl/fl}$;*Ndrg1*$^{CreERT2/+}$ mice injected with corn oil alone served as the controls (Conts). Mouse genotypes were confirmed using polymerase chain reaction. The primer sequences used for genotyping are listed in Supplementary Table S1.

General techniques

Histologic analyses, Western blotting, real-time polymerase chain reaction, brush border membrane (BBM) isolation, and *in vivo* analyses of PT endocytosis were performed using established protocols. The specific primer sets used for real-time polymerase chain reaction are listed in Supplementary Table S1. An antibody against the sodium-dependent phosphate cotransporter type 2a (NaPi-IIa; solute carrier transporter [SLC] 34A1) was generated as previously described.[19] All other antibodies used in this study were commercially available and are listed in Supplementary Tables S2 and S3. Additional methodological details are provided in the Supplementary Methods.

Statistical analyses

Comparisons between the 2 groups were performed using unpaired Student *t* tests for normally distributed data or Mann-Whitney *U* tests for nonnormally distributed data. Changes in dietary intake levels and body weight over time were analyzed using a linear mixed-effects model. Statistical analyses were conducted using GraphPad Prism 8.0 software (GraphPad Software) and EZR version 1.61 (Saitama Medical Center, Jichi Medical University), a graphical user interface for R (The R Foundation for Statistical Computing).[20] Data are presented as mean ± SD or median with interquartile range, as appropriate. $P < 0.05$ was considered statistically significant.

RESULTS

Syntaxin 3 is predominantly expressed in PTECs and localizes to the apical membrane in human and mouse kidneys

To identify the key syntaxin protein responsible for apical membrane trafficking in PTECs, we first analyzed the expression profiles of all syntaxin family members using publicly available single-nucleus RNA-sequencing data from human kidneys.[21,22] This analysis revealed that although several syntaxins are expressed, *STX3* showed the most prominent and specific expression in PT segments (Supplementary Figure S1). Other syntaxins expressed in the PT, such as *STX7* and *STX8*, are known to be primarily involved in endosome-to-lysosome trafficking and early endosomal regulation, respectively, rather than apical plasma membrane organization.[23,24] On the basis of this specific expression pattern, we prioritized syntaxin 3 for further investigation.

Although syntaxin 3 has been shown to localize to the apical membrane of PTECs in mouse kidneys, its distribution in human kidney tissues remains poorly characterized.[6,14] To address this, we examined the localization of syntaxin 3 in kidney biopsy samples from patients with minor glomerular abnormalities and in kidney sections from WT mice using immunofluorescence staining. In human samples, syntaxin 3 colocalized with *Lotus tetragonolobus* lectin, a marker of the apical brush border of PTECs (Figure 1a). Similarly, syntaxin 3 exhibited strong apical localization in the PTECs of WT mouse kidney sections (Figure 1b). To more definitively establish its PTEC-specific expression within the kidney cortex, we performed dual-immunofluorescence staining with markers for different tubular segments. This analysis revealed that syntaxin 3 expression is distinct from the distal tubule marker calbindin-D28k and the cortical collecting duct marker aquaporin-2 (Supplementary Figure S2).

Patients with MVID carrying *STX3* mutations exhibit Fanconi syndrome features

We analyzed blood and urine samples from 2 patients with MVID carrying distinct loss-of-function *STX3* mutations (Table 1). Patient 1 had a duplication mutation leading to a frameshift,[12,13,25] whereas patient 2 had a splice site mutation. Structural modeling predicts that both mutations result in severely truncated proteins lacking the essential SNARE and transmembrane domains, leading to a complete loss of function (Supplementary Figure S3).

Both patients presented with features consistent with Fanconi syndrome, although the specific manifestations varied. Patient 1 exhibited hypokalemia, hypophosphatemia, and urinary loss of phosphorus, glucose, low-molecular-weight proteins, and uric acid. In contrast, patient 2 presented with decreased plasma bicarbonate levels and generalized aminoaciduria (Tables 1 and 2). This phenotypic heterogeneity likely reflects a complex interplay of factors, including the different nature of the mutations, the patients' age, disease progression, and the influence of concurrent treatments, such as parenteral nutrition.

Although some blood abnormalities could be attributed to the primary intestinal dysfunction, the presence of specific

Figure 1 | (continued) magnifications. Individual staining for syntaxin 3 and *Lotus tetragonolobus* lectin (LTL) are shown in grayscale, whereas merged images display syntaxin 3 in red and LTL in green. (**b**) Immunofluorescence staining of wild-type (WT) mouse kidney tissue. Individual staining for syntaxin 3 and phalloidin shown in grayscale; merged images display syntaxin 3 in red and phalloidin in green. (**c**) Schematic illustration of the breeding strategy to generate PTEC-specific *Stx3*-cKO mice. *Ndrg1-Cre*^{ERT2} mice were crossed with *Stx3*$^{fl/fl}$ mice. Black triangles represent the *loxP* sites flanking exons 7 and 8 (gray rectangles) of the *Stx3* gene. *Cre*-mediated recombination results in the deletion of these exons in *Stx3*-cKO mice. (**d**) Western blot analysis of syntaxin 3 expression in the kidney cortex of control (Cont) and *Stx3*-cKO mice 1, 2, and 6 months after induction. Glyceraldehyde-3-phosphate dehydrogenase (GAPDH) served as loading control. (**e**) Immunofluorescence staining of Cont and *Stx3*-cKO mouse kidney tissue 2 months after induction, following the same staining pattern as (**b**). (**a,b,e**) Bars = 100 μm (low magnification) and 20 μm (high magnification). Images are representative of 3 independent experiments. To optimize viewing of this image, please see the online version of this article at www.kidney-international.org.

Table 1 | Clinical and laboratory characteristics of patients with MVID carrying *STX3* mutations

Characteristic	Patient 1	Patient 2	Reference
Demographics and genetics			
Sex	Male	Male	NA
Age, yr	10	3	NA
Mutation site of *STX3*	c.372_373dup	c.115-2A>G	NA
Treatment	On PPN	On TPN	NA
Serum tests			
Sodium, mEq/l	137	136	135–145
Potassium, mEq/l	3.5	4.2	3.5–5.1
Chloride, mEq/l	106	103	98–107
Calcium, mg/dl	NA	9.3	8.6–11.5
Phosphorus, mg/dl	2.8	4.7	3.3–5.6
Magnesium, mg/dl	2.2	NA	NA
Creatinine, mg/dl	0.41	0.14	0.26–0.42
Urea nitrogen, mg/dl	11.4	21.6	7.8–22.7
eGFR, ml/min per 1.73 m^2	112	242	NA
Uric acid, mg/dl	1.3	2.7	3.4–7.6
Glucose, mg/dl	74	76	65–100
Total protein, g/dl	7.1	7.8	6.0–8.0
Albumin, g/dl	3.4	4.5	3.8–5.4
Blood gas analysis			
pH	7.38	7.37	7.35–7.45
HCO_3^-, mmol/l	NA	19.0	22.0–29.0
Urinary tests			
Sodium, mmol/l	108	21	NA
Potassium, mmol/l	48	99	NA
Chloride, mmol/l	68	86	NA
Calcium, mg/dl	7	18	NA
Phosphorus, mg/dl	91	193	NA
Creatinine, mg/dl	11	70	NA
Uric acid, mg/dl	16	118	NA
Glucose, mg/dl	26	NA	NA
Protein, mg/dl	129	47	NA
Albumin, mg/dl	8	NA	NA
α1-Microglobulin, mg/l	187	NA	NA
β2-Microglobulin, mg/l	46	NA	NA
Vitamin D–binding protein, mg/l	>0.6[a]	NA	NA
Retinol-binding protein 4, mg/l	>3.3[a]	NA	NA
Fractional excretion, %			
Phosphorus	121.13	8.21	NA
Uric acid	45.87	8.72	NA

eGFR, estimated glomerular filtration rate; MVID, microvillus inclusion disease; NA, not available; PPN, peripheral parenteral nutrition; TPN, total parenteral nutrition.
[a]Values above the upper detection limit.
This table presents the demographic, genetic, and laboratory data of 2 patients with MVID caused by *STX3* mutations. Patient 1 presented with gastrointestinal dysfunction, growth retardation, metabolic abnormalities, mild hemostatic disorders, and severe retinal dysfunction. Patient age was reported at the time of data collection. The reference ranges shown are from the institution of patient 2.

Table 2 | Urinary amino acid analysis in a patient with MVID (patient 2)

Amino acid	Concentration, μmol/g creatinine	Reference, μmol/g creatinine
Alanine	1411	290–1020
α-Aminoadipic acid	391	0–30
α-Aminobutyric acid	125	0–50
Arginine	180	0–80
Asparagine	164	0–270
Aspartic acid	386	10–40
β-Alanine	655	0–40
β-Aminoisobutyric acid	854	0–1550
Citrulline	Not detected	0–50
Cystathionine	Not detected	0–10
Cystine	644	40–130
γ-Aminobutyric acid	223	0–110
Glutamic acid	348	0–90
Glutamine	1589	370–2090
Glycine	4127	980–2880
Histidine	2887	600–2250
Homocystine	104	0–100
Hydroxyproline	Not detected	0–110
Isoleucine	Not detected	0–50
Leucine	385	20–160
Lysine	817	90–410
Methionine	206	10–190
1-Methyl-histidine	292	0–350
3-Methyl-histidine	389	180–520
Ornithine	851	0–60
Phenylalanine	455	50–190
Phosphoethanolamine	1478	0–70
Phosphoserine	323	0–300
Proline	Not detected	0–80
Serine	2348	280–830
Taurine	13,125	110–1770
Threonine	880	90–420
Tryptophane	408	0–20
Tyrosine	450	90–270
Valine	238	20–180

MVID, microvillus inclusion disease.
This table presents the urinary amino acid profile of patient 2.

urinary abnormalities in both cases provided clear evidence of kidney PT dysfunction. We obtained data from 2 additional patients; however, they were excluded from this analysis because of severe dehydration or poor general condition. Despite the clinical differences between patients 1 and 2, these findings indicate that a functional loss of syntaxin 3 contributes to the development of Fanconi syndrome in humans.

Generation of PT-specific *Stx3* knockout mice

The *Stx3* gene in mice codes for 4 different splice forms (*Stx3a*, *Stx3b*, *Stx3c*, and *Stx3d*), with *Stx3a* being the only isoform expressed in kidney tissues.[26] We generated mice with floxed *Stx3* alleles ($Stx3^{fl/fl}$) in which exons 7 and 8, common to *Stx3a*, *Stx3b*, and *Stx3c* splice forms, were flanked by *loxP* sites (Supplementary Figure S4A). Systemic knockout was achieved through 2 different alleles: the targeted allele containing the neomycin cassette before flippase recognition target–mediated removal ($Stx3^{neo/neo}$), and the *Cre*-recombined allele generated by crossing with

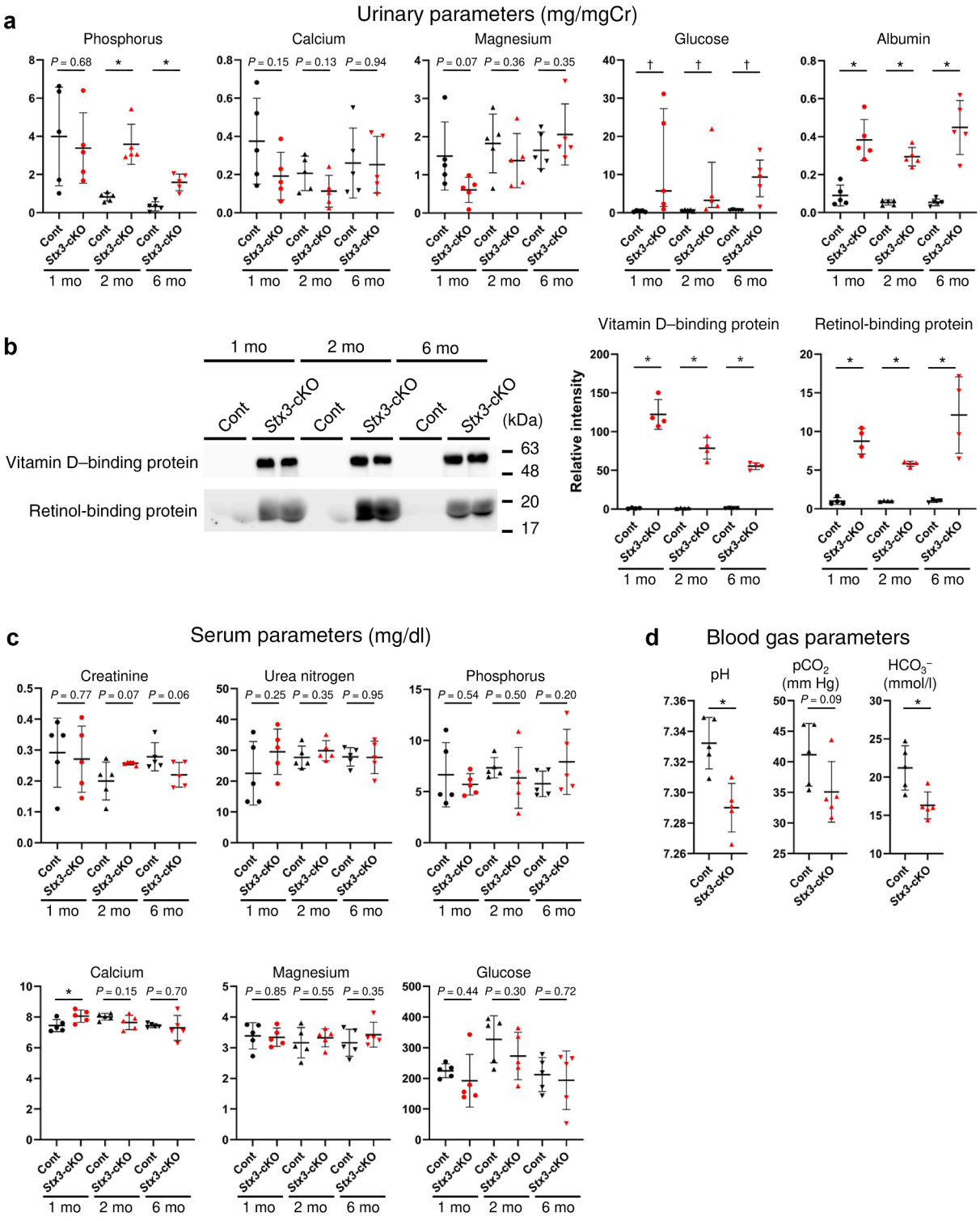

Figure 2 | *Stx3* conditional knockout (*Stx3*-cKO) mice develop a Fanconi syndrome phenotype. (**a**) Urinary excretion of phosphorus, calcium, magnesium, glucose, and albumin in control (Cont) and *Stx3*-cKO mice 1, 2, and 6 months after induction (n = 5 per group at each time point; *$P < 0.05$ using Student *t* test for phosphorus, calcium, magnesium, and albumin, †$P < 0.05$ using Mann-Whitney *U* test for glucose). (**b**) Left: Western blot analysis of urinary vitamin D–binding protein and retinol-binding protein. Urine samples were loaded after normalization to urinary creatinine levels. Right: Quantification of urinary protein levels (n = 4 per group at each time point; *$P < 0.05$ using Student *t* test). (**c**) Serum levels of creatinine (Cr), urea nitrogen, phosphorus, calcium, magnesium, and glucose in Cont and *Stx3*-cKO mice over time (n = 5 per group at each time point; *$P < 0.05$ using Student *t* test). (**d**) Blood gas parameters (pH, CO_2, and HCO_3^-) 2 months after induction (n = 5 per group; *$P < 0.05$ using Student *t* test). All quantitative results are presented as a scatterplot with mean ± SD, except for urinary glucose with median ± interquartile range.

Table 3 | Comparison of urinary amino acid concentrations in Cont and *Stx3*-cKO mice

Amino acid	Cont mice, µmol/g creatinine (n = 5)	*Stx3*-cKO mice, µmol/g creatinine (n = 5)	*P* value
Alanine	328 ± 42	1718 ± 1197	<0.05
α-Aminoadipic acid	179 ± 49	713 ± 380	<0.05
α-Aminobutyric acid	79 ± 32	132 ± 36	<0.05
Arginine	557 ± 120	884 ± 493	0.187
Asparagine	337 ± 76	640 ± 313	0.069
Aspartic acid	134 ± 42	180 ± 38	0.106
β-Alanine	507 ± 115	539 ± 59	0.598
β-Aminoisobutyric acid	253 ± 56	216 ± 23	0.207
Carnosine	37 ± 17	86 ± 51	0.073
Citrulline	120 ± 14	1699 ± 1906	0.101
Cystathionine	194 ± 66	512 ± 237	<0.05
Cystine	195 ± 92	1610 ± 1184	<0.05
Ethanolamine	3740 ± 210	2948 ± 188	<0.05
γ-Aminobutyric acid	359 ± 231	344 ± 61	0.891
Glutamic acid	270 ± 42	1119 ± 286	<0.05
Glutamine	1089 ± 208	12,303 ± 11,678	0.064
Glycine	1098 ± 125	7594 ± 6609	0.059
Histidine	205 ± 72	2387 ± 2086	<0.05
Homocystine	67 ± 97	49 ± 67	0.739
Hydroxy-lysine	436 ± 421	411 ± 395	0.927
Hydroxyproline	48 ± 47	337 ± 214	<0.05
Isoleucine	130 ± 28	538 ± 421	0.063
Leucine	573 ± 80	2801 ± 2217	0.055
Lysine	244 ± 45	468 ± 226	0.061
Methionine	253 ± 77	1769 ± 1316	<0.05
1-Methyl-histidine	676 ± 134	786 ± 107	0.191
3-Methyl-histidine	451 ± 103	569 ± 127	0.144
Ornithine	460 ± 75	682 ± 329	0.181
Phenylalanine	97 ± 25	246 ± 181	0.102
Phosphoethanolamine	362 ± 222	481 ± 174	0.373
Proline	44 ± 28	222 ± 109	<0.05
Sarcosine	0	176 ± 173	0.053
Serine	291 ± 90	1979 ± 1547	<0.05
Taurine	69,558 ± 10,868	58,474 ± 7468	0.097
Threonine	529 ± 121	5995 ± 5450	0.055
Tryptophane	29 ± 17	100 ± 79	0.087
Tyrosine	166 ± 32	1280 ± 1147	0.062
Valine	209 ± 42	860 ± 660	0.059

Cont, control; *Stx3*-cKO, *Stx3* conditional knockout.
This table presents the urinary amino acid profiles of Cont and *Stx3*-cKO mice 2 months after induction (n = 5 per group). The number of undetected samples was 1 for γ-aminobutyric acid (1 Cont), 6 for homocystine (3 Cont), 4 for hydroxy-lysine (2 Cont), 2 for hydroxyproline (2 Cont), 1 for proline (1 Cont), and 5 for sarcosine (5 Cont). Data are given as mean ± SD. *P* values were calculated using unpaired Student *t* tests.

cytomegalovirus–*Cre* mice ($Stx3^{-/-}$). When we examined the embryo on embryonic day 8.5, systemic knockout embryos ($Stx3^{neo/neo}$) were smaller than the heterozygotes littermates ($Stx3^{neo/+}$) (Supplementary Figure S4B). No systemic knockout ($Stx3^{-/-}$ or $Stx3^{neo/neo}$) pups were observed at postnatal day 0 (Supplementary Figure S4C). Thus, systemic deletion of *Stx3* leads to embryonic lethality.

Next, $Stx3^{fl/fl}$ mice were crossed with mice expressing tamoxifen-inducible *Cre* recombinase under the control of the *Ndrg1* promoter ($Ndrg1^{CreERT2/+}$) to generate PT-specific *Stx3*-cKO (Figure 1c and Supplementary Figure S5A). Tamoxifen treatment of the resulting offspring ($Stx3^{fl/fl}$; $Ndrg1^{CreERT2/+}$) induced *Cre*-mediated recombination and deletion of *Stx3*, specifically in PTECs (*Stx3*-cKO group). $Stx3^{fl/fl}$;$Ndrg1^{CreERT2/+}$ mice treated with corn oil alone served as the control (Cont group). Western blot analysis and immunofluorescence staining confirmed the successful and PTEC-specific depletion of *Stx3* in *Stx3*-cKO mice (Figure 1d and e and Supplementary Figure S5B–D). *Stx3*-cKO mice showed no significant differences in food intake or body weight compared with Cont mice (Supplementary Figure S5E).

Stx3-cKO mice develop the Fanconi syndrome phenotype

Analysis of urine and serum parameters in Cont and *Stx3*-cKO mice 1, 2, and 6 months after induction revealed a Fanconi syndrome phenotype in *Stx3*-cKO mice. These mice exhibited significantly increased urinary excretion of phosphorus, glucose, and albumin compared with Cont mice at all time points, except for the urinary excretion of phosphorus 1 month after induction (Figure 2a). Urinary calcium and magnesium levels were not different between the 2 groups. Western blot analysis of urine samples showed a marked increase in low-molecular-weight protein excretion in *Stx3*-cKO mice (Figure 2b). Additionally, *Stx3*-cKO mice displayed increased urinary amino acid excretion (Table 3). Serum analysis showed no significant differences in most parameters between Cont and *Stx3*-cKO mice, except for calcium levels 1 month after induction (Figure 2c), suggesting compensatory homeostatic mechanisms. However, *Stx3*-cKO mice exhibited significant decreases in blood pH and bicarbonate (HCO_3^-) levels, with decreased carbon dioxide (CO_2) levels (Figure 2d), indicating metabolic acidosis, another feature of Fanconi syndrome.

PTECs in *Stx3*-cKO mice show specific apical trafficking defects without signs of mitochondrial or lysosomal dysfunction

Morphologic analysis of PTECs from *Stx3*-cKO mice revealed significant structural changes primarily at the apical pole. Periodic acid–Schiff staining revealed brush border atrophy (Figure 3a and b). Transmission electron microscopy analysis provided a detailed quantification of these ultrastructural changes. Specifically, *Stx3*-cKO mice showed a significant reduction in both microvilli length and number, whereas overall cell height and the number of basolateral interdigitations were unaffected, indicating the structural defect was confined to the apical region (Table 4). Concurrently, there was a marked increase in the number of subapical vesicles, along with the presence of ectopic brush borders (Figure 3c and Table 4).

Given that other forms of Fanconi syndrome are known to arise from distinct cellular pathologies—such as primary

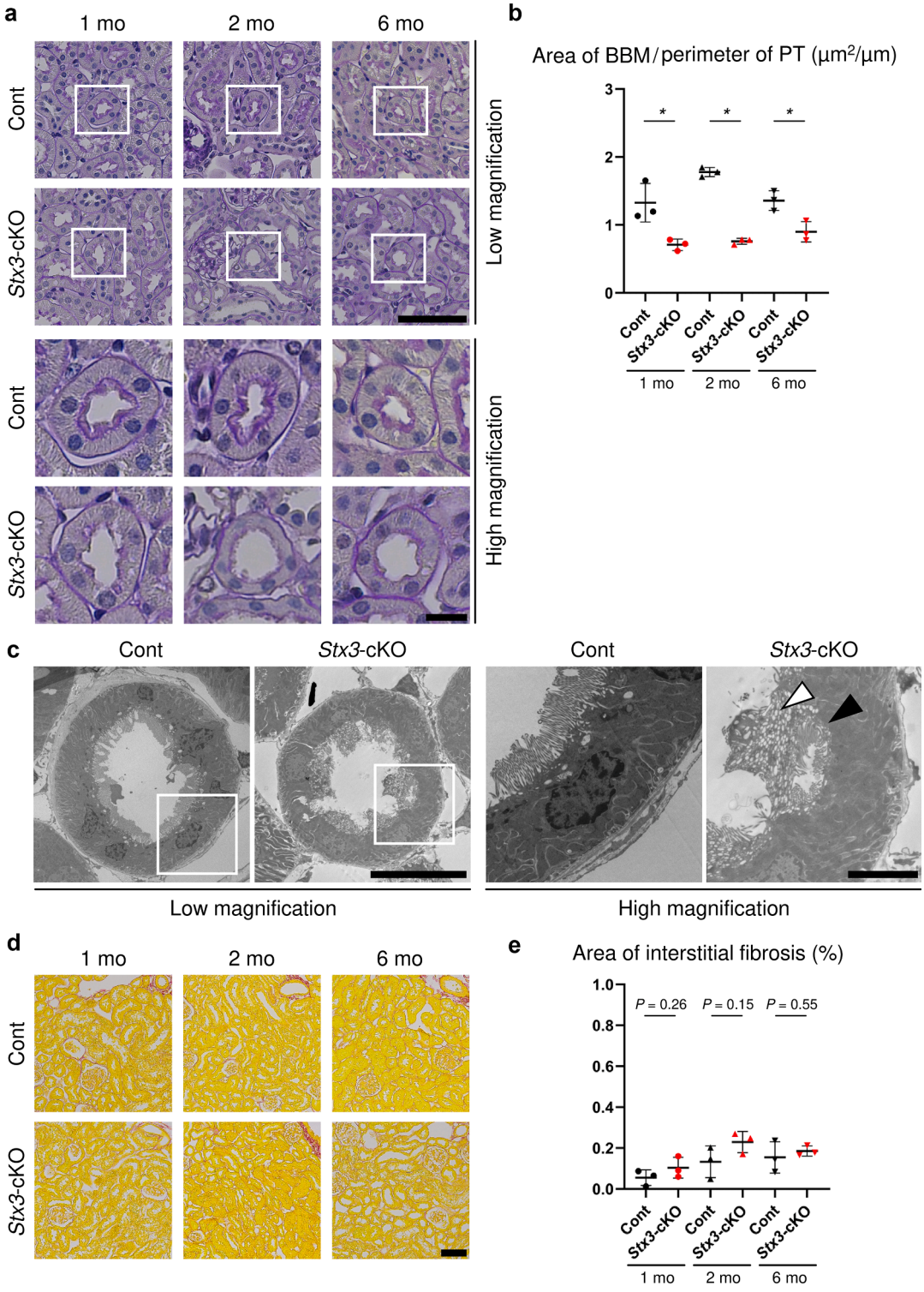

Figure 3 | *Stx3* conditional knockout (*Stx3*-cKO) mice exhibit brush border atrophy and microvillus inclusions in proximal tubule (PT) epithelial cells (PTECs). (**a**) Periodic acid–Schiff–stained kidney sections from control (Cont) and *Stx3*-cKO mice 1, 2, and 6 months after induction. White boxes in low-magnification images (top) indicate areas shown at high magnification (bottom). Bars = 100 μm (low magnification) and 20 μm (high magnification). (**b**) Quantification of the brush border area per tubule perimeter (n = 3 per group; $^*P < 0.05$ using Student *t*test). (**c**) Transmission electron microscopy images of PTECs 1 month after induction. White squares in low-magnification images (left) are enlarged on the right. In *Stx3*-cKO mice, accumulation of vesicles (white arrowheads) and ectopic brush borders (black arrowheads) were observed. Bars = 20 μm (low magnification) and 5 μm (high magnification). (**d**) Picrosirius red–stained kidney sections from Cont and *Stx3*-cKO mice. Bar: 100 μm. (**e**) Quantification of the fibrotic area in kidney sections stained with picrosirius red (n = 3 per group; Student *t* test). All quantitative results are presented as a scatterplot with mean ± SD. BBM, brush border membrane. To optimize viewing of this image, please see the online version of this article at www.kidney-international.org.

Table 4 | Quantification analysis of morphometric parameters of PTECs using electron microscopy images

Parameters	Cont mice	*Stx3*-cKO mice	*P* value
Cell height, μm	9.94 ± 1.14	10.13 ± 1.11	0.804
Microvilli length, μm	2.92 ± 0.24	1.12 ± 0.10	<0.001
No. of microvilli/luminal perimeter, /μm	7.30 ± 0.56	4.93 ± 0.62	<0.001
No. of basolateral interdigitation/basolateral perimeter, /μm	1.70 ± 0.49	1.70 ± 0.22	0.998
Mitochondrial area/cell area, %	23.9 ± 4.72	22.7 ± 3.47	0.643
No. of vesicles/cell area, /μm^2	0.19 ± 0.05	0.98 ± 0.23	<0.001

Cont, control; PTEC, proximal tubule epithelial cell; *Stx3*-cKO, *Stx3* conditional knockout.
This table presents comparison of the morphometric parameters of PTECs of Cont and *Stx3*-cKO mice 1 month after induction (n = 5 per group). Data are given as mean ± SD. *P* values were calculated using unpaired Student *t* tests.

mitochondrial damage, lysosomal dysfunction, or impaired autophagy—we next investigated whether these pathways were affected in *Stx3*-cKO mice.[27–29] Because mitochondrial damage can often trigger apoptosis, we assessed both mitochondrial integrity and programmed cell death. We found that mitochondrial respiratory chain function, evaluated by succinate dehydrogenase and cytochrome *c* oxidase staining, was preserved (Supplementary Figure S6A and B). This was consistent with our ultrastructural analysis, which showed a comparable mitochondrial area relative to total cell area (Table 4). In line with these findings of preserved mitochondrial integrity, evaluation of cleaved caspase-3 showed no significant difference between Cont and *Stx3*-cKO mice (Supplementary Figure S6C). Furthermore, markers for lysosomal integrity (lysosomal associated membrane protein 1 [LAMP1]) and autophagy flux (p62/sequestosome-1 [SQSTM1]) also showed no significant alterations (Supplementary Figure S6D and E).

We also examined the expression of markers for kidney injury, inflammation, and fibrosis at the transcriptional level at 2 months after induction. Although *Havcr1* mRNA was slightly elevated in *Stx3*-cKO mice, the magnitude of this increase was minor compared with that typically observed in models of overt kidney injury (Supplementary Figure S7).[30] Moreover, the expression of other markers, including key inflammatory and fibrotic genes, remained unchanged between the groups.

Consistent with a specific, nonpleiotropic defect, picrosirius red staining indicated no apparent fibrosis in *Stx3*-cKO kidneys up to 6 months after induction (Figure 3d and e). To confirm that this lack of severe pathology persisted long-term, we extended our observation period to 9 months, which again revealed no evidence of progressive kidney failure (Supplementary Figure S8). Taken together, these results indicate that the tubulopathy in *Stx3*-cKO mice is caused by a specific disruption of apical trafficking machinery, rather than a secondary consequence of mitochondrial, lysosomal, or general metabolic failure.

Stx3-cKO mice exhibit impaired expression and localization of transporters and receptors associated with Fanconi syndrome in PTECs

We investigated the expression and localization of apical transporters and receptors associated with the development of Fanconi syndrome. NaPi-IIa, sodium-glucose cotransporter 2 (SGLT2; SLC5A2), megalin (low density lipoprotein receptor-related protein 2 [LRP2]), sodium/hydrogen exchanger 3 (NHE3), and related to $b^{0,+}$ amino acid transport protein (rBAT; SLC3A1) were evaluated as potential causes of increased urinary excretion of phosphorus, glucose, and low-molecular-weight proteins, metabolic acidosis, and aminoaciduria, respectively. Additionally, we examined the distribution of ezrin, a protein that links the plasma membrane to the actin cytoskeleton and has been reported to bind directly to syntaxin 3.[31]

Immunofluorescence staining revealed that in Cont mice, these proteins were localized to the apical membrane of PTECs, albeit with distinct distribution patterns within the apical domain (Figures 4 and 5, Supplementary Figures S9 and S10, and Table 5). NaPi-IIa, SGLT2, rBAT, and ezrin were predominantly distributed in brush border regions in Cont mice (negative values on the *x* axis in Figure 5). In contrast, NHE3 showed a peak distribution at the base of the brush border (*x*-axis position 0 in Figure 5), whereas megalin exhibited a peak localization slightly below the base of the brush border in Cont mice (slightly positive values on the *x* axis in Figure 5). In *Stx3*-cKO mice, NaPi-IIa, NHE3, and megalin were internalized from their normal locations, whereas SGLT2, rBAT, and ezrin showed decreased expression rather than localization shifts (Table 5).

Western blotting of BBMs confirmed decreased apical expression of NaPi-IIa, SGLT2, and NHE3 in *Stx3*-cKO mice, whereas no significant changes were detected in megalin, rBAT, and ezrin expression (Figure 4g). However, quantitative analysis of immunofluorescence images revealed contrasting results; in *Stx3*-cKO mice, megalin expression decreased in the apical region and increased in the basolateral region, and rBAT showed a marked reduction in the apical region (Table 5 and Figure 5). This apparent discrepancy can be attributed to methodological differences. Immunofluorescence analysis allows precise spatial quantification of protein distribution, whereas BBM isolation is inherently less spatially selective and likely includes regions slightly posterior to the brush border base, as evidenced by numerous previous studies that successfully detected megalin fractions.[32,33] Furthermore, both megalin and rBAT are abundantly expressed in the S3 segment of the PTs,[34,35] which is less affected by the *Ndrg1*$^{CreERT2/+}$-mediated knockout that primarily targets the S1 and S2 segments.[18] Ezrin, a protein crucial for maintaining microvillar structure by directly linking actin filaments to the plasma membrane, showed similarly distinct results between the analytical methods. Although immunofluorescence revealed decreased expression in *Stx3*-cKO mice (Figure 5f), the BBM fractions showed unchanged levels (Figure 4g). This difference likely reflects

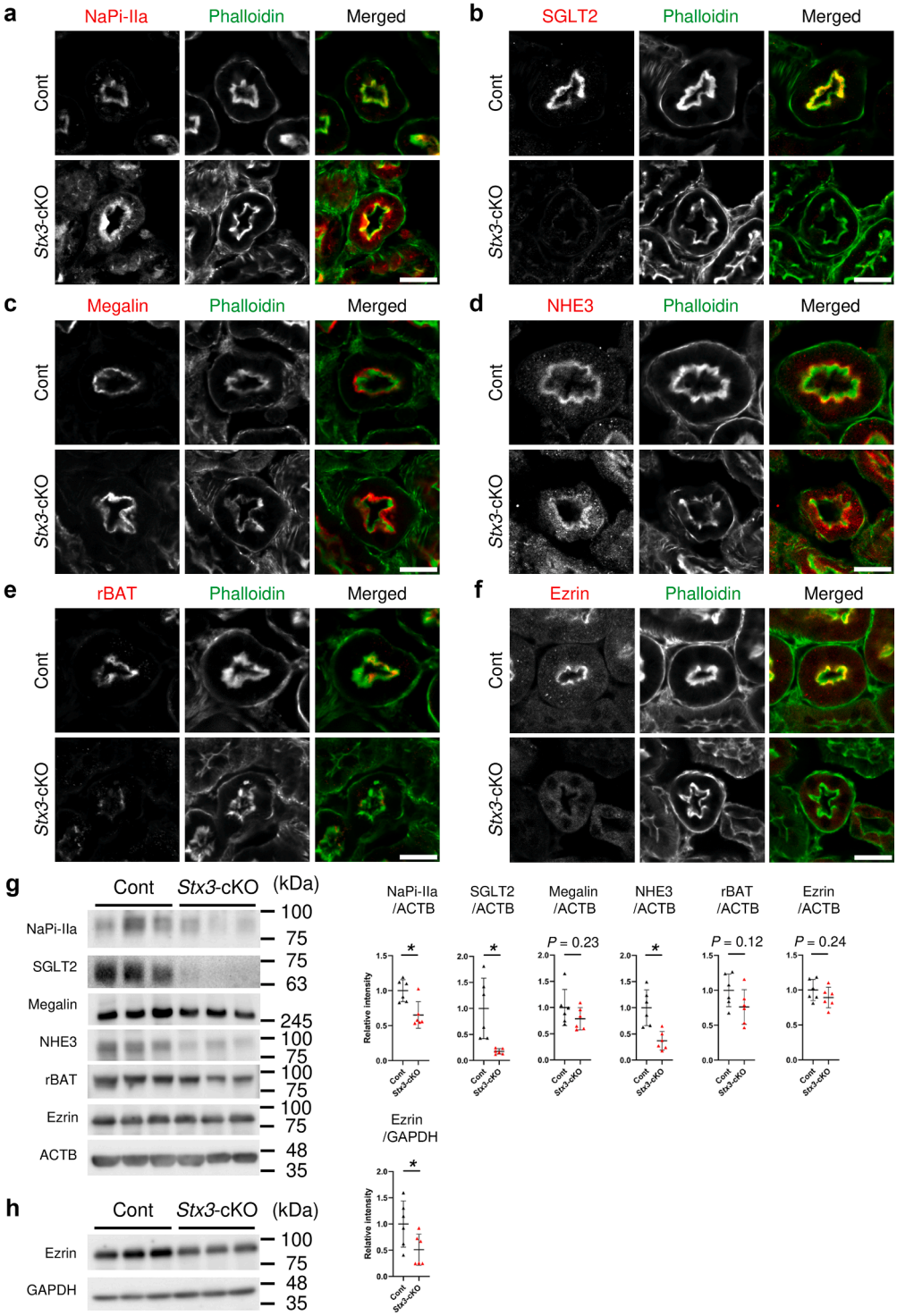

Figure 4 | Loss of syntaxin 3 disrupts the expression and localization of key apical membrane proteins in proximal tubule epithelial cells. (**a–f**) Immunofluorescence staining of kidney cortex sections from control (Cont) and *Stx3* conditional knockout (*Stx3*-cKO) mice 2 months after induction. Representative images show the distribution of (**a**) sodium-dependent phosphate cotransporter type 2a (NaPi-IIa), (**b**) sodium-glucose cotransporter 2 (SGLT2), (**c**) megalin, (**d**) sodium/hydrogen exchanger 3 (NHE3), (**e**) related to $b^{0,+}$ amino acid transport protein (rBAT), and (**f**) ezrin (left; grayscale), with F-actin visualized using phalloidin staining (middle; grayscale). Merged images (right) show the proteins of interest in red and phalloidin in green. Bars = 20 μm. (**g**) Western blot analysis of isolated brush border membranes from Cont and *Stx3*-cKO mice 2 months after induction. β-Actin (ACTB) served as a loading control. (**h**) Western blot analysis of total kidney cortex lysates from the same mice, with glyceraldehyde-3-phosphate dehydrogenase (GAPDH) as a loading control. Quantification of protein levels from (**g**) and (**h**), normalized to their respective loading controls (n = 6 per group; *$P < 0.05$ using Student *t* test). Data are presented as scatterplots with mean ± SD. To optimize viewing of this image, please see the online version of this article at www.kidney-international.org.

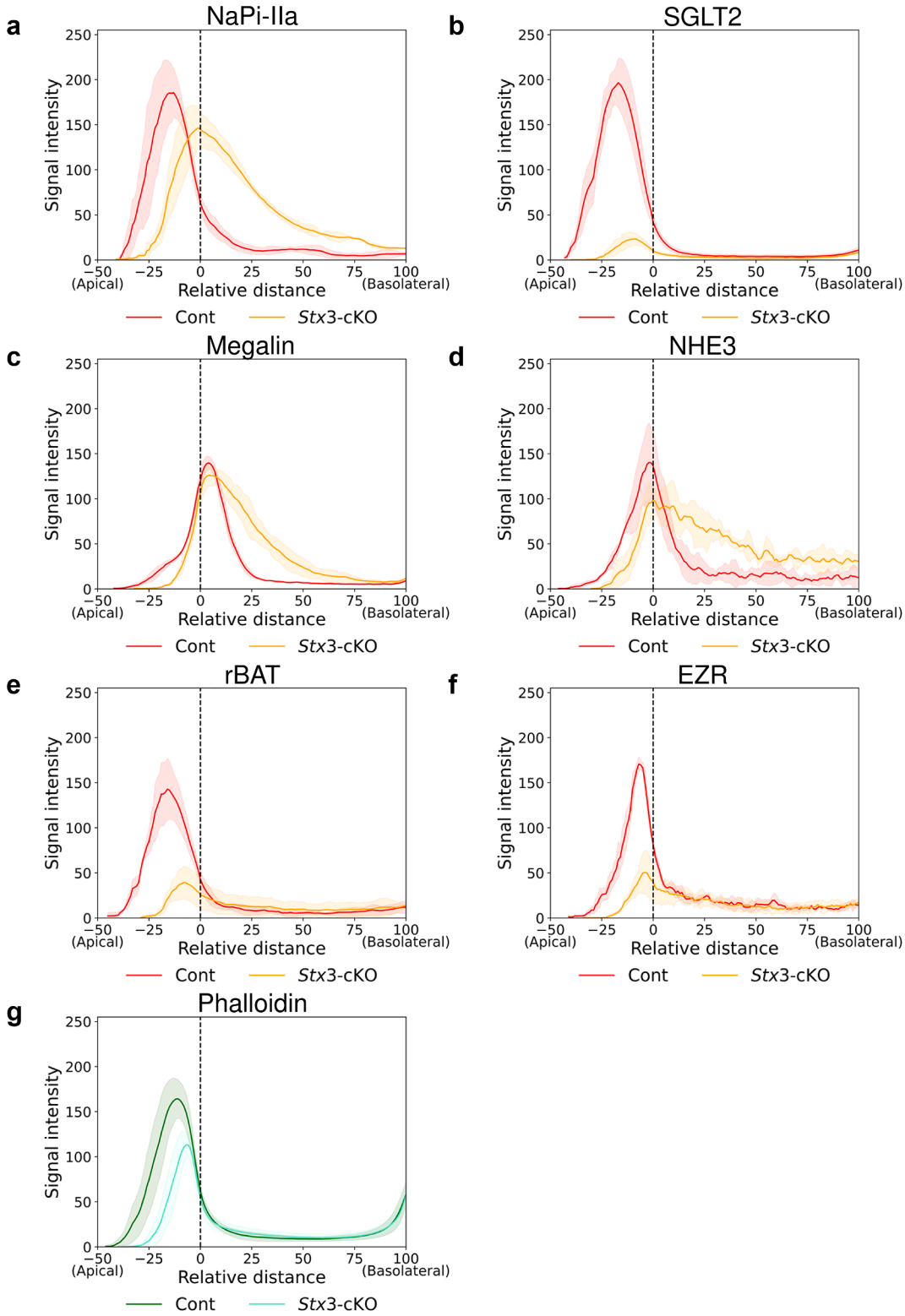

Figure 5 | Quantitative distribution profiles of key apical membrane proteins in proximal tubule epithelial cells based on immunofluorescence analysis. The protein distribution was quantified using the method described in Supplementary Figure S9. For the key apical membrane proteins shown in Figure 4, the red and orange lines represent control (Cont) and *Stx3* conditional knockout (*Stx3*-cKO) mice, respectively. For phalloidin staining, the green and cyan lines represent Cont and *Stx3*-cKO mice, respectively. Data represent mean ± SD intensity from 3 mice per group for membrane proteins and from 18 mice for phalloidin. EZR, ezrin; NaPi-IIa, sodium-dependent phosphate cotransporter type 2a; NHE3, sodium/hydrogen exchanger 3; rBAT, related to $b^{0,+}$ amino acid transport protein; SGLT2, sodium-glucose cotransporter 2.

Table 5 | Quantitative analysis of protein distribution in PTECs using area under the curve measurements

	Apical area		Basolateral area	
Variable	Cont mice	*Stx3*-cKO mice	Cont mice	*Stx3*-cKO mice
NaPi-IIa	4363 ± 1046	2242 ± 653	1306 ± 376	5387 ± 207
	($P < 0.05$)		($P < 0.05$)	
SGLT2	4759 ± 565	409 ± 149	673 ± 213	335 ± 68
	($P < 0.05$)		($P = 0.06$)	
Megalin	1156 ± 56	650 ± 84	2522 ± 194	4431 ± 720
	($P < 0.05$)		($P < 0.05$)	
NHE3	2016 ± 350	971 ± 357	2405 ± 1133	5093 ± 982
	($P < 0.05$)		($P < 0.05$)	
rBAT	3275 ± 583	600 ± 280	939 ± 421	1191 ± 924
	($P < 0.05$)		($P = 0.689$)	
Ezrin	2522 ± 211	575 ± 192	1848 ± 394	1652 ± 677
	($P < 0.05$)		($P = 0.687$)	
Phalloidin	3932 ± 535	1726 ± 381	1565 ± 352	1744 ± 449
	($P < 0.05$)		($P = 0.192$)	

Cont, control; NaPi-IIa, sodium-dependent phosphate cotransporter type 2a; NHE3, sodium/hydrogen exchanger 3; PTEC, proximal tubule epithelial cell; rBAT, related to $b^{0,+}$ amino acid transport protein; SGLT2, sodium-glucose cotransporter 2; *Stx3*-cKO, *Stx3* conditional knockout.
The area under the curve was used to quantitatively analyze the protein distribution in PTECs. Signal intensity profiles from Figure 5 were divided into 2 regions: the apical area (negative values on the *x* axis, from −50 to 0) and the basolateral area (positive values on the *x* axis, from 0 to 100), with the brush border base defined as position 0. Values represent mean ± SD from 3 mice per group, except for phalloidin staining, where data were pooled from all experimental groups (n = 18). Statistical comparisons between Cont and *Stx3*-cKO mice were performed using unpaired Student *t* test.

the BBM isolation process, which enriches the structurally intact brush border structures. Because ezrin is essential for brush border formation, the BBM fraction represents protein levels only in the remaining intact brush border regions. Western blot analysis of whole cortical lysates confirmed decreased ezrin expression in *Stx3*-cKO mice, consistent with the immunofluorescence findings (Figure 4h).

Real-time polymerase chain reaction analyses of kidney cortex tissues showed no changes in the mRNA expression levels of these receptors and transporters, suggesting that the alterations observed using immunostaining and Western blotting were due to post-translational regulation (Supplementary Figure S11). The localization of Na^+/K^+-ATPase α1, a key molecule expressed on the basolateral membrane of PTs that generates the Na^+/K^+ gradient driving NaPi-IIa and SGLT2 function, remained unchanged (Supplementary Figures S12). This suggests that syntaxin 3 is not involved in basolateral polarity.

Syntaxin 3 deficiency leads to the accumulation of trafficking molecules in the subapical region

The SNARE complex comprises target-SNARE and vesicle-SNARE proteins. Previous studies have shown that several SNARE proteins localize to the apical membrane of PTECs. These include the vesicle-SNARE protein vesicle-associated membrane protein 8 (VAMP8) and the target-SNARE protein synaptosome-associated protein 23 (SNAP23), which have been detected in rat PTECs.[6,36] Additionally, these proteins—VAMP8, SNAP23, and syntaxin 3—have been shown to form a functional SNARE complex during granule fusion in pancreatic cells.[9] On the basis of these findings, we compared VAMP8 and SNAP23 expression levels between Cont and *Stx3*-cKO mice PTECs.

Immunofluorescence analysis revealed an increased accumulation of VAMP8 in the subapical region of *Stx3*-cKO mice (Figure 6a). The expression of SNAP23 showed no differences between Cont and *Stx3*-cKO mice (Figure 6b). Previous studies have demonstrated that syntaxin 3 functions within the Rab cascade, with Rab11 mediating the fusion of transport vesicles to the plasma membrane.[37] Therefore, we examined Rab11 expression in PTECs. In Cont mice, Rab11 was localized to the apical region of the PTECs, whereas *Stx3*-cKO mice showed enhanced Rab11 expression in this region (Figure 6c). Western blot analysis of kidney cortex lysates confirmed the immunofluorescence results (Figure 6d). The enhanced expression of VAMP8 and Rab11 in the subapical region suggested the accumulation of transport vesicles immediately beneath the apical plasma membrane, which is consistent with our transmission electron microscopy observations (Figure 3c). Given the established role of Rab11-positive vesicles in megalin recycling, we examined megalin distribution relative to Rab11 and early endosome antigen 1 to analyze its trafficking pathway.[38] Superresolution imaging revealed increased megalin colocalization with Rab11 in the subapical region of *Stx3*-cKO mice, whereas early endosome antigen 1–positive vesicles remained unchanged (Figure 6e–g). These findings indicate impaired megalin recycling without alterations in early endosome vesicles, suggesting compromised functional efficiency.

Both receptor-mediated endocytosis and fluid-phase endocytosis were impaired in the PTECs of *Stx3*-cKO mice

Receptor-mediated endocytosis and fluid-phase endocytosis are crucial for the reabsorption of PTECs from the glomerular filtrate. Receptor-mediated endocytosis primarily

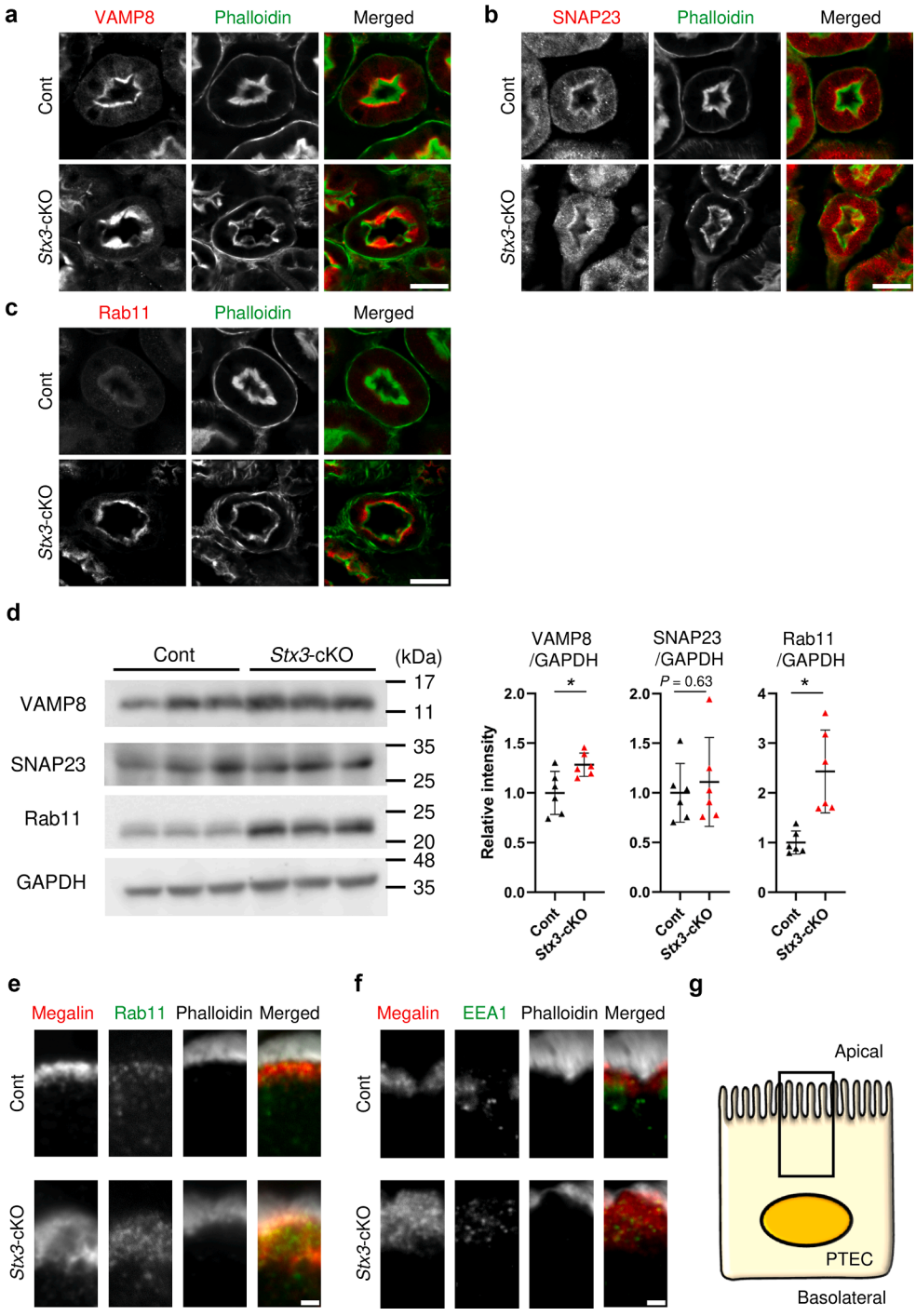

Figure 6 | Syntaxin 3 deficiency leads to subapical accumulation of specific vesicular trafficking proteins in proximal tubule epithelial cells (PTECs). (**a–c**) Immunofluorescence analysis of kidney cortex sections from control (Cont) and *Stx3* conditional knockout (*Stx3*-cKO) mice 2 months after induction. Distribution of vesicular trafficking-related proteins (**a**) vesicle-associated membrane protein 8 (VAMP8), (**b**) synaptosome-associated protein 23 (SNAP23), and (**c**) Rab11 (left; grayscale) is shown with F-actin visualization using phalloidin staining (middle; grayscale). Merged images (right) show trafficking proteins in red and F-actin in green. Bars = 20 μm. (**d**) Western blot analysis of total kidney cortex lysates (left) and quantification of protein levels normalized to glyceraldehyde-3-phosphate dehydrogenase (GAPDH) (right) (n = 6 per group; $*P < 0.05$ using Student *t* test). Data are presented as scatterplots with mean ± SD. (**e,f**) Superresolution immunofluorescence images of the apical and subapical regions of PTECs from Cont and *Stx3*-cKO mice 2 months after induction. Images show megalin (left; grayscale), vesicular trafficking–related proteins (**e**) Rab11 and (**f**) early endosome antigen 1 (EEA1) (middle-left; grayscale), and F-actin (phalloidin; middle-right; grayscale). Merged images (right) show megalin in red, trafficking proteins in green, and F-actin in grayscale. Bars = 1 μm. (**g**) Schematic diagram showing the imaging regions for panels (**e**) and (**f**), indicated by black rectangles. To optimize viewing of this image, please see the online version of this article at www.kidney-international.org.

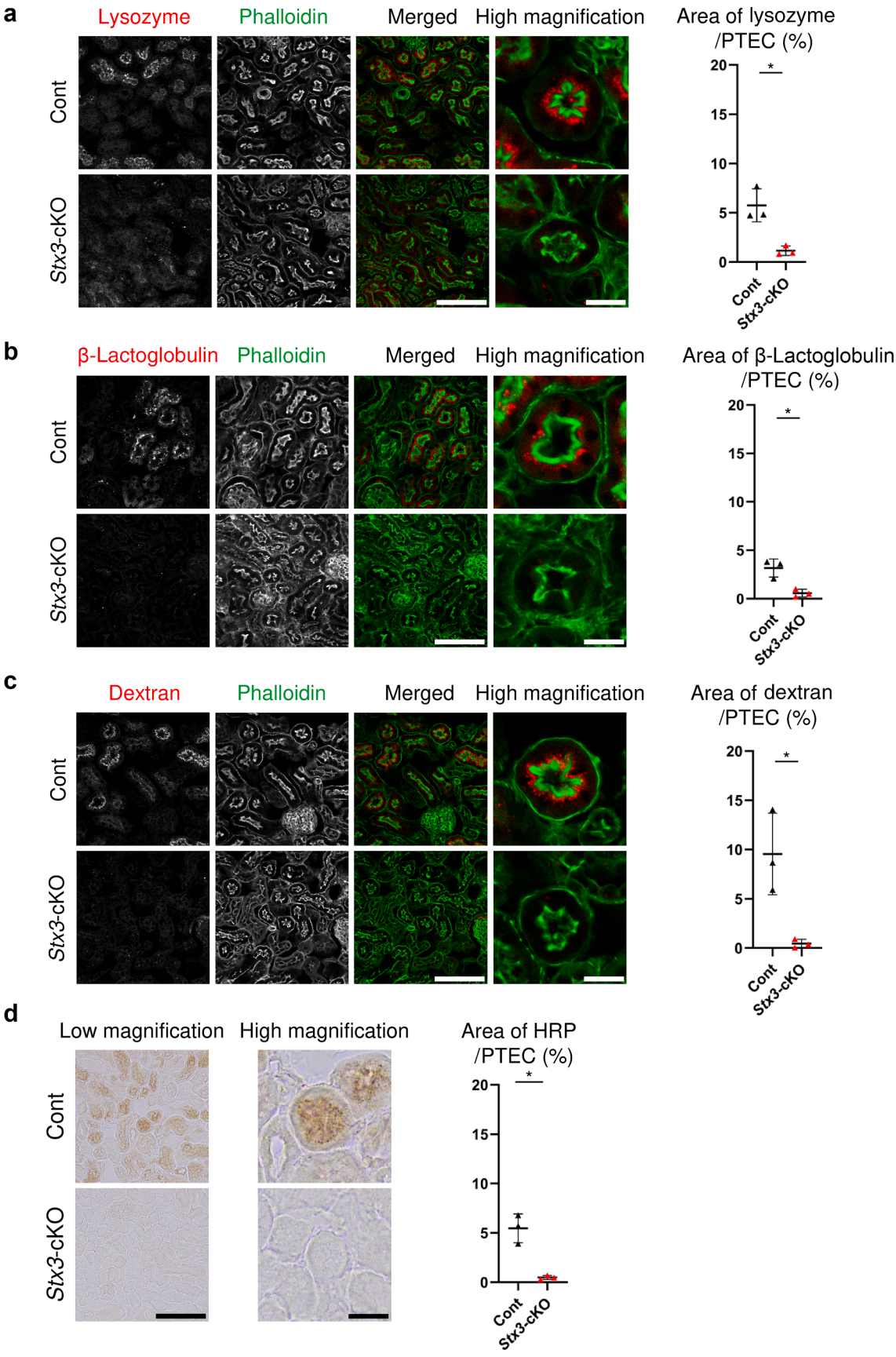

Figure 7 | Loss of syntaxin 3 impairs both receptor-mediated and fluid-phase endocytosis in proximal tubules. (**a–c**) Assessment of endocytic uptake in the kidney of control (Cont) and *Stx3* conditional knockout (*Stx3*-cKO) mice 10 minutes after i.v. (continued)

involves the megalin-cubilin receptor complex, whereas fluid-phase endocytosis involves actin-driven membrane ruffling and macropinosome formation.[4,39] The elevated levels of urinary low-molecular-weight proteins observed in a patient with MVID (Table 1), increased urinary vitamin D binding protein and retinol binding protein in *Stx3*-cKO mice, and abnormal localization of megalin in the *Stx3*-cKO mice suggested impaired receptor-mediated endocytosis due to syntaxin 3 dysfunction. To directly assess the dysfunction of receptor-mediated endocytosis in the *Stx3*-cKO mice, we i.v. administered lysozyme or β-lactoglobulin to the mice and evaluated their uptake into PTECs. *Stx3*-cKO mice exhibited significantly reduced uptake of these molecules, confirming the impairment of receptor-mediated endocytosis (Figure 7a and b). Next, we examined the impact of syntaxin 3 deficiency on fluid-phase endocytosis. Fluorescently labeled dextran (10 kDa) or horseradish peroxidase was administered i.v. The uptake of both molecules markedly decreased in the PTECs of *Stx3*-cKO mice, indicating impaired fluid-phase endocytosis (Figure 7c and d). These findings collectively demonstrate that syntaxin 3 is essential for both receptor-mediated and fluid-phase endocytosis in PTECs.

DISCUSSION

This study demonstrated, for the first time, the critical role of syntaxin 3 in maintaining PTEC function and preventing Fanconi syndrome. Our findings in *Stx3*-cKO mice not only provide strong evidence that syntaxin 3 dysfunction leads to a Fanconi syndrome phenotype but also confirm *in vivo* its role in epithelial cell polarity regulation, which was previously only evidenced in cultured cell studies.[7] These results, coupled with observations from patients with MVID carrying *STX3* mutations, validate and extend our understanding of the function of syntaxin 3 in epithelial cells.

The development of Fanconi syndrome in *Stx3*-cKO mice appears to be multifactorial, involving a complex interplay between impaired trafficking and localization of key transporters and receptors, and disruptions in both receptor-mediated and fluid-phase endocytosis on the apical surface of PTECs. Both abnormal distribution and impaired recycling of receptors, particularly megalin, directly contribute to the defective receptor-mediated endocytosis of low-molecular-weight proteins. The abnormal localization of NaPi-IIa and NHE3, along with reduced expression of SGLT2 and rBAT, leads to urinary loss of phosphorus, glucose, and amino acids, and acidemia. Impaired actin organization, likely resulting from disrupted interactions between syntaxin 3 and ezrin, affects multiple aspects of PTEC function. The actin-rich brush border, which is critical for increasing the apical surface area of PTECs, was significantly shortened in *Stx3*-cKO mice, further compromising PTEC function. Consequently, fluid-phase endocytosis, particularly macropinocytosis, which depends on dynamic actin remodeling for membrane ruffling and vesicle formation, was also severely impaired. This impairment appears to stem from at least 2 key syntaxin 3–dependent defects: (i) compromised actin organization due to decreased ezrin expression (Figures 4f and 5f), which is critical for linking the actin cytoskeleton to the apical membrane and is implicated in macropinocytosis[40]; and (ii) critically, the mislocalization of NHE3 from the apical membrane (Figures 4d and 5d). This loss of proper apical NHE3 localization is expected to disrupt the regulation of submembranous pH, a process demonstrated to be essential for the precise actin polymerization and remodeling required for efficient macropinosome formation.[31,41]

In *Stx3*-cKO mice, we observed intriguing differential responses of various transporters to STX3 deficiency, despite unchanged mRNA expression levels. SGLT2 and rBAT showed decreased fluorescence intensity, whereas NaPi-IIa, megalin, and NHE3 shifted to a subapical localization. This likely reflects the distinct regulatory mechanisms inherent to each transporter. NaPi-IIa and NHE3 are subject to rapid hormone-mediated regulation on a minute-to-minute basis, allowing for dynamic control of phosphorus and sodium reabsorption in response to physiological demands.[3,42] Similarly, megalin-mediated endocytosis relies heavily on efficient receptor recycling for continuous protein reabsorption from glomerular filtrates.[4] In contrast, SGLT2 and rBAT, which are responsible for the near-complete reabsorption of filtered glucose and amino acids, do not appear to undergo such rapid regulation, at least to the best of our knowledge.[43] This fundamental difference in the temporal control of these transporters suggests that NaPi-IIa, NHE3, and megalin rely more heavily on recycling mechanisms for their regulation, potentially explaining the observed differences in immunofluorescence patterns.

The Fanconi syndrome observed in our *Stx3*-cKO model allows comparison with other genetic tubulopathies presenting similar phenotypes. Although these conditions all cause generalized PT dysfunction, the underlying molecular pathways are distinct, highlighting the specific role of syntaxin 3. (i) Our model's pathophysiology—primary failure of apical vesicle fusion—differs mechanistically from Dent

Figure 7 | (continued) administration of receptor-mediated endocytosis markers (**a**) Cy5-lysozyme and (**b**) Alexa555–β-lactoglobulin) or a fluid-phase marker (**c**) Texas Red–dextran. For each row: administered molecule (left), F-actin (phalloidin; middle-left), merged image (middle-right), and high-magnification view (right). In the merged images, administered molecules are shown in red and F-actin in green. Bars = 100 μm (left 3 panels) and 20 μm (right panel). Representative images of the proximal tubule from 3 independent experiments are shown. Graphs show uptake quantification per proximal tubule epithelial cell (PTEC) area (n = 3 per group; $^*P < 0.05$ using Student *t* test). (**d**) Fluid-phase endocytosis assessed by horseradish peroxidase (HRP) uptake. Representative images at low (left) and high (right) magnification. Bars = 100 μm (left) and 20 μm (right). The graph shows the quantification of HRP-positive area per PTEC (n = 3 per group; $^*P < 0.05$ using Student *t* test). All data are presented as scatterplots with mean ± SD. To optimize viewing of this image, please see the online version of this article at www.kidney-international.org.

disease, caused by mutations in the endosomal chloride channel *CLCN5*. In Dent disease, defective endosomal acidification and maturation disrupt receptor recycling within the endocytic pathway.[44] This mechanistic difference explains their distinct long-term outcomes: progressive kidney failure in *Clcn5* knockout mice results from significant hypercalciuria, promoting nephrocalcinosis and inflammation.[45] In contrast, our *Stx3*-cKO mice do not develop hypercalciuria, explaining the lack of disease progression. (ii) The syntaxin 3 pathway also differs from cystinosis, where defective lysosomal transporter *CTNS* causes cystine accumulation, constitutive mammalian target of rapamycin complex 1 activation, and cellular reprogramming toward proliferation.[28] Our model shows more limited effects than deletion of master regulators, like mammalian target of rapamycin complex 1 or vacuolar protein sorting (VPS) 34, whose ablation causes pleiotropic effects, disrupting cell growth, metabolism, and autophagy, leading to a broader cellular collapse.[29,46] (iii) Our *Stx3*-cKO mice maintain normal mitochondrial morphology and function, distinguishing them from tubulopathies with primary mitochondrial damage, such as in *Gatm*-mutant models.[27] Therefore, the lack of progression to kidney failure provides key mechanistic insight: pure apical trafficking defects are sufficient to cause Fanconi syndrome but do not trigger the globally damaging pathways leading to kidney failure in other models.

Our findings in both patients with MVID and *Stx3*-cKO mice suggest that kidney manifestations in MVID may be an underrecognized component of the disease. MVID is a genetically heterogeneous disorder; although mutations in *MYO5B* were initially identified as the primary cause, variants in *STX3* or *STXBP2* are known to cause similar intestinal symptoms.[13,47,48] Kidney involvement in MVID has been previously reported in patients with *MYO5B* mutations.[49] However, the findings are inconsistent, with some patients showing Fanconi syndrome, whereas others report no kidney abnormalities.[50] To the best of our knowledge, this is the first report of Fanconi syndrome demonstrated in patients with MVID carrying *STX3* mutations. The phenotypic variability observed across different MVID subtypes likely arises from a complex interplay of factors. These include not only the specific genetic defect—the affected gene and the nature of the mutation—but also the patient's age and developmental stage, which alter metabolic demands, and the masking effects of severe diarrhea, such as malnutrition and electrolyte imbalances.[51] Given that chronic urinary solute wasting in children can lead to significant growth and bone complications, our findings underscore the importance of monitoring patients with MVID, particularly those with *STX3* mutations, for signs of kidney tubular dysfunction.

Our study had several limitations. The rarity of MVID, particularly that caused by *STX3* mutations, restricted our clinical observations to only 2 patients. However, investigating the molecular basis of rare genetic diseases, like MVID, is crucial for understanding fundamental biological processes and developing potential therapeutic strategies.

In conclusion, this study demonstrated the critical role of syntaxin 3 in maintaining PTEC function and apical polarity. Our results not only bridge the gap between *in vitro* and *in vivo* observations in epithelial cell biology but also suggest new avenues for managing MVID. Future research on SNARE complex dynamics in PTECs may provide further insights into the maintenance of epithelial cell polarity and the identification of potential therapeutic targets for both MVID and Fanconi syndrome.

DISCLOSURE

All the authors declared no competing interests.

DATA STATEMENT

All data generated or analyzed during this study are included in this published article and its supplementary information files.

ACKNOWLEDGMENTS

The authors would like to thank Ms. Naoko Horimoto for her technical assistance.

FUNDING STATEMENT

This study was supported by Dr. Tomoaki Mizuno, Dr. Eiji Oiki, and the Center for Medical Research and Education, Graduate School of Medicine, The University of Osaka. This work is supported by grants from the Ichiro Kanehara Foundation (2022), the Kidney Foundation, Japan (JKFB22-8), and the Osaka Kidney Foundation (OKF24-0011).

AUTHOR CONTRIBUTIONS

HO performed conceptualization, data curation, formal analysis, investigation, methods, visualization, and writing (original draft) and acquired funding. KI performed conceptualization, data curation, formal analysis, investigation, methods, validation, and writing (original draft) and acquired funding. AI, AM, and NT performed investigation and writing (review and editing). MK and NI obtained resources and performed writing (review and editing). RA curated data, obtained resources, and performed writing (review and editing). YAR and SAS curated data, obtained resources, and performed writing (review and editing). TY and MM performed writing (review and editing). AH and MY obtained resources and performed writing (review and editing). YI acquired funding acquisition and performed project administration, supervision, and writing (review and editing). IM performed conceptualization, investigation, methods, project administration, supervision, and writing (review and editing).

Supplementary material is available online at www.kidney-international.org.

REFERENCES

1. Chrysopoulou M, Rinschen MM. Metabolic rewiring and communication: an integrative view of kidney proximal tubule function. *Annu Rev Physiol*. 2024;86. annurev-physiol-042222-024724.
2. Ghezzi C, Loo DDF, Wright EM. Physiology of renal glucose handling via SGLT1, SGLT2 and GLUT2. *Diabetologia*. 2018;61:2087–2097.
3. Bacic D, LeHir M, Biber J, et al. The renal Na+/phosphate cotransporter NaPi-IIa is internalized via the receptor-mediated endocytic route in response to parathyroid hormone. *Kidney Int*. 2006;69:495–503.
4. Christensen EI, Birn H. Megalin and cubilin: multifunctional endocytic receptors. *Nat Rev Mol Cell Biol*. 2002;3:258–267.

5. Lemaire M. Novel Fanconi renotubular syndromes provide insights in proximal tubule pathophysiology. *Am J Physiol Renal Physiol*. 2021;320:F145–F160.
6. Li X, Low SH, Miura M, et al. SNARE expression and localization in renal epithelial cells suggest mechanism for variability of trafficking phenotypes. *Am J Physiol Renal Physiol*. 2002;283:F1111–F1122.
7. Sharma N, Low SH, Misra S, et al. Apical targeting of syntaxin 3 is essential for epithelial cell polarity. *J Cell Biol*. 2006;173:937–948.
8. Frank SPC, Thon KP, Bischoff SC, et al. SNAP-23 and syntaxin-3 are required for chemokine release by mature human mast cells. *Mol Immunol*. 2011;49:353–358.
9. Behrendorff N, Dolai S, Hong W, et al. Vesicle-associated membrane protein 8 (VAMP8) is a SNARE (soluble N-ethylmaleimide-sensitive factor attachment protein receptor) selectively required for sequential granule-to-granule fusion. *J Biol Chem*. 2011;286:29627–29634.
10. Low SH, Chapin SJ, Wimmer C, et al. The SNARE machinery is involved in apical plasma membrane trafficking in MDCK cells. *J Cell Biol*. 1998;141:1503–1513.
11. Sanchez E, Gonzalez EA, Moreno DS, et al. Syntaxin 3, but not syntaxin 4, is required for mast cell–regulated exocytosis, where it plays a primary role mediating compound exocytosis. *J Biol Chem*. 2019;294:3012–3023.
12. Janecke AR, Liu X, Adam R, et al. Pathogenic STX3 variants affecting the retinal and intestinal transcripts cause an early-onset severe retinal dystrophy in microvillus inclusion disease subjects. *Hum Genet*. 2021;140:1143–1156.
13. Wiegerinck CL, Janecke AR, Schneeberger K, et al. Loss of syntaxin 3 causes variant microvillus inclusion disease. *Gastroenterology*. 2014;147:65–68.e10.
14. Lehtonen S, Riento K, Olkkonen VM, et al. Syntaxin 3 and Munc-18-2 in epithelial cells during kidney development. *Kidney Int*. 1999;56:815–826.
15. Shi S, Ma K, Bin NR, et al. Syntaxin-3 is dispensable for basal neurotransmission and synaptic plasticity in postsynaptic hippocampal CA1 neurons. *Sci Rep*. 2020;10:709.
16. Schwartz GJ, Munoz A, Schneider MF, et al. New equations to estimate GFR in children with CKD. *J Am Soc Nephrol*. 2009;20:629–637.
17. Sato T, Mushiake S, Kato Y, et al. The Rab8 GTPase regulates apical protein localization in intestinal cells. *Nature*. 2007;448:366–369.
18. Endo T, Nakamura J, Sato Y, et al. Exploring the origin and limitations of kidney regeneration. *J Pathol*. 2015;236:251–263.
19. Yasuda S, Inoue K, Matsui I, et al. Hepatic phosphate uptake and subsequent nerve-mediated phosphaturia are crucial for phosphate homeostasis following portal vein passage of phosphate in rats. *Sci Rep*. 2023;13:5794.
20. Kanda Y. Investigation of the freely available easy-to-use software "EZR" for medical statistics. *Bone Marrow Transplant*. 2013;48:452–458.
21. Wu H, Malone AF, Donnelly EL, et al. Single-cell transcriptomics of a human kidney allograft biopsy specimen defines a diverse inflammatory response. *J Am Soc Nephrol*. 2018;29:2069–2080.
22. Wu H, Uchimura K, Donnelly EL, et al. Comparative analysis and refinement of human PSC-derived kidney organoid differentiation with single-cell transcriptomics. *Cell Stem Cell*. 2018;23:869–881.e8.
23. Mullock BM, Smith CW, Ihrke G, et al. Syntaxin 7 is localized to late endosome compartments, associates with Vamp 8, and is required for late endosome–lysosome fusion. *Mol Biol Cell*. 2000;11:3137–3153.
24. Subramaniam VN, Loh E, Horstmann H, et al. Preferential association of syntaxin 8 with the early endosome. *J Cell Sci*. 2000;113:997–1008.
25. Schillemans M, Karampini E, Van Den Eshof BL, et al. Weibel-Palade body localized syntaxin-3 modulates von Willebrand factor secretion from endothelial cells. *Arterioscler Thromb Vasc Biol*. 2018;38:1549–1561.
26. Curtis LB, Doneske B, Liu X, et al. Syntaxin 3b is a t-SNARE specific for ribbon synapses of the retina. *J Comp Neurol*. 2008;510:550–559.
27. Reichold M, Klootwijk ED, Reinders J, et al. Glycine amidinotransferase (GATM), renal Fanconi syndrome, and kidney failure. *J Am Soc Nephrol*. 2018;29:1849–1858.
28. Berquez M, Chen Z, Festa BP, et al. Lysosomal cystine export regulates mTORC1 signaling to guide kidney epithelial cell fate specialization. *Nat Commun*. 2023;14:3994.
29. Rinschen MM, Harder JL, Carter-Timofte ME, et al. VPS34-dependent control of apical membrane function of proximal tubule cells and nutrient recovery by the kidney. *Sci Signal*. 2022;15:eabo7940.
30. Hammoud S, Ivanova A, Osaki Y, et al. Tubular CPT1A deletion minimally affects aging and chronic kidney injury. *JCI Insight*. 2024;9:e171961.
31. Yu H, Zhou J, Takahashi H, et al. Spatial control of proton pump H,K-ATPase docking at the apical membrane by phosphorylation-coupled ezrin-syntaxin 3 interaction. *J Biol Chem*. 2014;289:33333–33342.
32. Yammani RR, Sharma M, Seetharam S, et al. Loss of albumin and megalin binding to renal cubilin in rats results in albuminuria after total body irradiation. *Am J Physiol Regul Integr Comp Physiol*. 2002;283:R339–R346.
33. Yamagata M, Ozono K, Hashimoto Y, et al. Intraperitoneal administration of recombinant receptor-associated protein causes phosphaturia via an alteration in subcellular distribution of the renal sodium phosphate co-transporter. *J Am Soc Nephrol*. 2005;16:2338–2345.
34. Christensen EI, Kristoffersen IB, Grann B, et al. A well-developed endolysosomal system reflects protein reabsorption in segment 1 and 2 of rat proximal tubules. *Kidney Int*. 2021;99:841–853.
35. Pfeiffer R, Loffing J, Rossier G, et al. Luminal heterodimeric amino acid transporter defective in cystinuria. *Mol Biol Cell*. 1999;10:4135–4147.
36. Inoue T, Nielsen S, Mandon B, et al. SNAP-23 in rat kidney: colocalization with aquaporin-2 in collecting duct vesicles. *Am J Physiol Renal Physiol*. 1998;275:F752–F760.
37. Knowles BC, Weis VG, Yu S, et al. Rab11a regulates syntaxin 3 localization and microvillus assembly in enterocytes. *J Cell Sci*. 2015;128:1617–1626.
38. Perez Bay AE, Schreiner R, Benedicto I, et al. The fast-recycling receptor megalin defines the apical recycling pathway of epithelial cells. *Nat Commun*. 2016;7:11550.
39. Polesel M, Hall AM. Axial differences in endocytosis along the kidney proximal tubule. *Am J Physiol Renal Physiol*. 2019;317:F1526–F1530.
40. D'Angelo R, Aresta S, Blangy A, et al. Interaction of ezrin with the novel guanine nucleotide exchange factor PLEKHG6 promotes RhoG-dependent apical cytoskeleton rearrangements in epithelial cells. *Mol Biol Cell*. 2007;18:4780–4793.
41. Koivusalo M, Welch C, Hayashi H, et al. Amiloride inhibits macropinocytosis by lowering submembranous pH and preventing Rac1 and Cdc42 signaling. *J Cell Biol*. 2010;188:547–563.
42. Hu MC, Fan L, Crowder LA, et al. Dopamine acutely stimulates Na+/H+exchanger (NHE3) endocytosis via clathrin-coated vesicles. *J Biol Chem*. 2001;276:26906–26915.
43. Park SH, Belcastro E, Hasan H, et al. Angiotensin II-induced upregulation of SGLT1 and 2 contributes to human microparticle-stimulated endothelial senescence and dysfunction: protective effect of gliflozins. *Cardiovasc Diabetol*. 2021;20:65.
44. Piwon N, Günther W, Schwake M, et al. ClC-5 Cl–channel disruption impairs endocytosis in a mouse model for Dent's disease. *Nature*. 2000;408:369–373.
45. Cebotaru V, Kaul S, Devuyst O, et al. High citrate diet delays progression of renal insufficiency in the ClC-5 knockout mouse model of Dent's disease. *Kidney Int*. 2005;68:642–652.
46. Grahammer F, Ramakrishnan SK, Rinschen MM, et al. mTOR regulates endocytosis and nutrient transport in proximal tubular cells. *J Am Soc Nephrol*. 2017;28:230–241.
47. Dhekne HS, Pylypenko O, Overeem AW, et al. *MYO5B, STX3*, and *STXBP2* mutations reveal a common disease mechanism that unifies a subset of congenital diarrheal disorders: a mutation update. *Hum Mutat*. 2018;39:333–344.
48. Stepensky P, Bartram J, Barth TF, et al. Persistent defective membrane trafficking in epithelial cells of patients with familial hemophagocytic lymphohistiocytosis type 5 due to *STXBP2/MUNC18-2* mutations. *Pediatr Blood Cancer*. 2013;60:1215–1222.
49. Golachowska MR, van Dael CML, Keuning H, et al. MYO5B mutations in patients with microvillus inclusion disease presenting with transient renal Fanconi syndrome. *J Pediatr Gastroenterol Nutr*. 2012;54:491–498.
50. Schlegel C, Weis VG, Knowles BC, et al. Apical membrane alterations in non-intestinal organs in microvillus inclusion disease. *Dig Dis Sci*. 2018;63:356–365.
51. Okposio MM, Onyiriuka AN, Abhulimhen-Iyoha BI. Point-of-admission serum electrolyte profile of children less than five years old with dehydration due to acute diarrhoea. *Trop Med Health*. 2015;43:247–252.